Soft Matter

PAPER

Check for updates

Cite this: *Soft Matter*, 2021, **17**, 10649

A continuum membrane model can predict curvature sensing by helix insertion†

Yiben Fu,[a] Wade F. Zeno,[b] Jeanne C. Stachowiak[c] and Margaret E. Johnson*[a]

Protein domains, such as ENTH (epsin N-terminal homology) and BAR (bin/amphiphysin/rvs), contain amphipathic helices that drive preferential binding to curved membranes. However, predicting how the physical parameters of these domains control this 'curvature sensing' behavior is challenging due to the local membrane deformations generated by the nanoscopic helix on the surface of a large sphere. We here use a deformable continuum model that accounts for the physical properties of the membrane and the helix insertion to predict curvature sensing behavior, with direct validation against multiple experimental datasets. We show that the insertion can be modeled as a local change to the membrane's spontaneous curvature, c_0^{ins}, producing excellent agreement with the energetics extracted from experiments on ENTH binding to vesicles and cylinders, and of ArfGAP helices to vesicles. For small vesicles with high curvature, the insertion lowers the membrane energy by relieving strain on a membrane that is far from its preferred curvature of zero. For larger vesicles, however, the insertion has the inverse effect, de-stabilizing the membrane by introducing more strain. We formulate here an empirical expression that accurately captures numerically calculated membrane energies as a function of both basic membrane properties (bending modulus κ and radius R) as well as stresses applied by the inserted helix (c_0^{ins} and area A_{ins}). We therefore predict how these physical parameters will alter the energetics of helix binding to curved vesicles, which is an essential step in understanding their localization dynamics during membrane remodeling processes.

Received 14th September 2021,
Accepted 11th November 2021

DOI: 10.1039/d1sm01333e

rsc.li/soft-matter-journal

I. Introduction

The recruitment of cytosolic proteins to membranes is an essential step in a variety of membrane remodeling processes, including clathrin-mediated endocytosis[1] and cell division.[2,3] Proteins that participate in membrane remodeling contain membrane binding domains that use positively charged interfaces to specifically target negatively charged lipids such as PI(4,5)P_2 on cell membranes.[4–6] In addition to this electrostatic interaction, these proteins exploit additional mechanisms, including helix insertion, scaffolding, crowding, and entropy gain by disordered proteins.[7–10] These mechanisms cause proteins to bind more strongly to more highly curved membranes, driving them to both sense and induce membrane curvature.[11] Amphipathic α-helices are common protein domains that are frequently found in peripheral membrane proteins like septins, epsins, endophilins, and amphiphysins. Playing key remodeling roles in cell division and endocytosis, these proteins insert themselves into a single leaflet of a membrane, where they can sense curvature independently of any additional curvature sensing mechanisms.[9] The stronger binding of helix-containing domains to membranes of high curvature can thus control their localization dynamics, helping to regulate subsequent steps in assembly and remodeling. Understanding how the strength of membrane binding depends on helix insertion and membrane properties is thus an essential component of predicting the spatial control of protein localization and corresponding remodeling dynamics.

Several lines of experimental evidence support curvature sensing by amphipathic helices and its direct coupling to membrane deformations and membrane energy changes. Tethered vesicle assays visualize increased binding to highly curved membranes for domains with α-helix.[9,12] Without the α-helix present, these same domains are insensitive to membrane curvature, demonstrating the significance of the helix in curvature sensing. The insertion or the α-helix changes the membrane local curvature and induces curvature generation.[13–15] Equilibrium observations of proteins bound to small unilamellar vesicles (SUVs) can be converted into dissociation constants by determining the relative partitioning of proteins to smaller vesicles (Fig. 1A). These dissociation constants can then be used to extract

[a] *T. C. Jenkins Department of Biophysics, The Johns Hopkins University, 3400 N. Charles St., Baltimore, Maryland 21218, USA. E-mail: margaret.johnson@jhu.edu*
[b] *Mork Family Department of Chemical Engineering and Materials Science, The University of Southern California, Los Angeles, California, 90089, USA*
[c] *Department of Biomedical Engineering, The University of Texas at Austin, Austin, Texas 78712, USA*

† Electronic supplementary information (ESI) available. See DOI: 10.1039/d1sm01333e

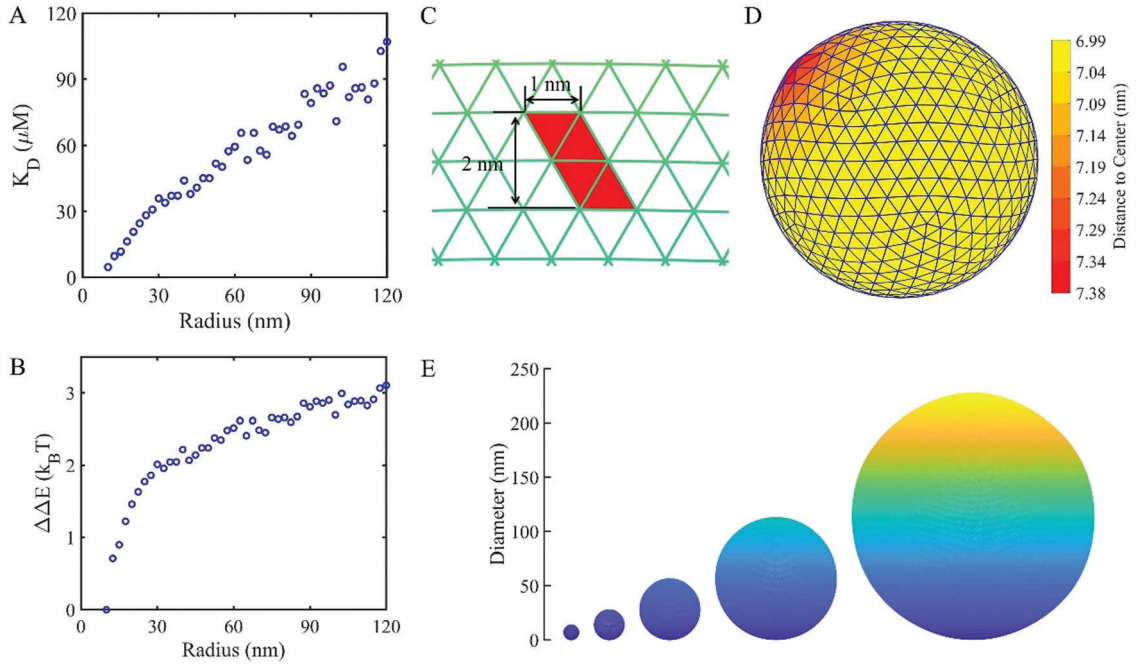

Fig. 1 Experimental curvature sensing by ENTH domains with amphipathic helices and the corresponding model design to quantify these results. (A) The dissociation constant of the amphipathic helix-containing ENTH domain is stronger with more highly curved (smaller) vesicles. The solution concentration of the ENTH domain is 150 nM and the PI(4,5)P_2 density on the vesicle is 0.125 nm^{-2}. (B) From the K_D, we can measure the difference in binding energy with vesicle size, using the smallest vesicle as the zero point. The positive energy changes reflect weaker binding. (C) The helix insertion is modeled as occupying four adjacent triangles on the vesicle surface (R = 7 nm), which are assigned a nonzero spontaneous curvature, c_0^{ins}, while the rest of the surface has a spontaneous curvature of zero. (D) The insertion modifies the membrane energy, with equilibrated structures deforming to produce local bulges that increase with larger c_0^{ins}. Here c_0^{ins} = 0.4 nm^{-1} and the color bar shows the distance of triangular face to the center of the vesicle. (E) Five vesicles of different sizes in our simulations. The vesicle radii are 7 nm, 14 nm, 28 nm, 56 nm and 112 nm from left to right.

changes of energy upon binding (Fig. 1B). This data on ENTH binding to vesicles provides a basis for our modeling comparison, where we can then address how the key parameters of curvature, bending modulus, tension, insertion size, and spontaneous curvature control membrane energies following helix insertion. As further validation for this modeling approach, we perform similar comparisons with experimental measurements of binding of the ArfGAP1 ALPS motifs on vesicles,[16] and of ENTH binding to cylindrical membrane tethers.[17]

Modeling and simulation using other approaches have illuminated several ways in which helix insertion alters membrane structure and stress. Molecular dynamics simulations have measured depth and orientation of helices in bilayers, deformations of the surface and lipid structure,[18,19] and corresponding changes to membrane stress around the insertion.[20] However, these simulations are limited to relatively small (nanometer scale) and typically flat membranes. Curved all-atom membranes have shown that the underlying deformation matches molecular factors, like protein shape,[21] but measurements of the energy changes arising from helices inserted into membranes of varying curvature have remained intractable using molecular dynamics. In contrast, models that use elasticity theory have quantified how stress profiles and energetics[22] in initially curved membranes will respond to helix insertion differentially, depending on how the curvature was generated and the depth of the insertion.[13] However, the modeled membrane patch varies with only two variables (thickness in one dimension, arc length in the other dimension), whereas our modeled vesicles exist in 3D space. These elasticity calculations thus only capture variation along one axis of principal curvature on a surface, assuming translational symmetry along the other. They cannot directly model spherical vesicles, where a highly localized and anisotropic insertion will impact curvature along both principal axes.

Deformable continuum membrane surfaces are an attractive model for studying membrane mechanics because they can adopt diverse geometries in 3D space, and their shape and energy will relax in response to perturbations. The calculations are relatively efficient, typically taking on the order of minutes or days depending on surface size (see Methods), *vs.* molecular simulations, where protein binding energy calculations would only be computationally tractable on the smallest of vesicles. Continuum membranes capture how the material bending modulus of the membrane, the membrane tension, and osmotic pressure will impact energetics and membrane shape.[23] Local perturbations driven by proteins adsorbed to the surface can be modeled *via* changes to the membrane's spontaneous curvature c_0, with values that can vary from 0 to $\sim$1 nm^{-1}.[24] The spontaneous curvature can vary spatially across the membrane surface, driving changes in membrane shape and tension,[25] thus providing an effective material parameter that captures changes to membrane stress on the outer *vs.* inner bilayer leaflets.[24]

 This journal is © The Royal Society of Chemistry 2021

Even before protein adsorption, any asymmetries in lipid composition between the inner and outer leaflets can contribute to a nonzero spontaneous curvature across the bilayer surface,[26] since each lipid has its own spontaneous curvature (see ref. 27). Continuum models can capture this asymmetry, as we show below, by specifying an initial spontaneous curvature to the bilayer, prior to any insertion. Continuum models can be coupled to models with attached and diffusing proteins[28–30] to capture interactions that drive membrane-mediated collective behavior,[31] or response of cell-shape to flow.[32] Thus, these models provide a flexible platform for integrating mechanical responses with environmental changes or biochemical interactions. We apply this detailed curvature model here to protein curvature sensing, showing that changing the local spontaneous curvature is an effective parameter for capturing a helix insertion.

In this paper, we first describe the model design, and the approach used to compare model results with *in vitro* experiments measuring surface coverage on SUVs of varying curvature. We then show how the spontaneous curvature of the insertion, c_0^{ins}, and the bending modulus κ have dominant effects on the membrane energy changes following insertion. Both the size and spread of the insertion further modulate the magnitude of the energy changes. In contrast, constraints on the area and volume that would arise due to area compressibility and osmotic pressure have minimal impact on controlling energetic responses to insertion. With these results we are able to define parameter regimes that produce excellent agreement with the experimental observations of curvature sensing. We validate that the results are robust to our numerical methods, including mesh size, integration scheme, and optimization protocol. We then recapitulate curvature sensing by helices reported in experiments on ENTH binding to membrane tethers and ALPS motifs binding to vesicles, also showing that the model reproduces stronger binding to membranes with higher diacylglycerol content.[33] Finally, through our numerical results we derive an empirical formula that predicts how membrane energies will change following insertion as a function of variations in c_0^{ins}, κ, radius and insertion area. This expression can thus be used to estimate curvature sensing by amphipathic helices without additional computational measurements, and we show it provides an excellent model fit to curvature sensing observed by the eAH and aAH helices.[9]

II. Model design

Continuum membrane model

The membrane is modeled using a continuum thin-film surface captured *via* a triangular mesh using the subdivision limit surface method[23] (Fig. 1). Given $\mathcal{M}$ as the membrane surface that is parameterized by curvilinear coordinates s_1 and s_2, the position $\boldsymbol{s}$ of each point on the surface in three-dimensional space ($\boldsymbol{s} \in \mathbb{R}^3$) is given by $\boldsymbol{s} = \boldsymbol{s}(s_1,s_2)$. The energy of the membrane is due to a bending energy (*via* the Helfrich Hamiltonian[34]) and constraints on the volume V and area A, defined as:[23]

$$E = \int_{\mathcal{M}} \frac{1}{2}\kappa[2H(\boldsymbol{s}) - c_0(\boldsymbol{s})]^2\sqrt{a}ds_1ds_2 + \frac{1}{2}\mu_{\mathrm{A}}\frac{(A-A_0)^2}{A_0} + \frac{1}{2}\mu_{\mathrm{V}}\frac{(V-V_0)^2}{V_0} + E_{\mathrm{reg}} \quad (1)$$

The first bending energy term integrates over all positions $\boldsymbol{s}$ on the surface $\mathcal{M}$, where $\sqrt{a} = \left\|\frac{\partial \boldsymbol{s}}{\partial s_1} \times \frac{\partial \boldsymbol{s}}{\partial s_2}\right\|$. The energy varies with mean curvature, $H(\boldsymbol{s})$, and the spontaneous curvature of the membrane, $c_0(\boldsymbol{s})$, where κ is the constant bending modulus. $H(\boldsymbol{s})$ is the mean of the calculated curvature summed along the two principal axes at point $\boldsymbol{s}$; for a sphere of radius R, it is a constant $1/R$ at all points. For a cylinder, the mean curvature is $1/2R$. $H(\boldsymbol{s})$ thus changes when the membrane deforms. $c_0(\boldsymbol{s})$ is zero for membrane bilayers (without proteins attached) when both leaflets have the same lipid composition. The second and third terms capture the area and volume constraints, with respective coefficients μ_{A} and μ_{V}. A is the membrane area, A_0 is the target area of the membrane, V is the vesicle volume, and V_0 is the target volume of the vesicle. The fourth term is the regularization energy, E_{reg}, which is added to eliminate the in-plane shearing deformations of the triangular mesh as the structure is optimized. This technical rather than physical constraint (due to the numerical mesh) should go to zero in equilibrated structures, and in Methods we describe specific forms we tested to minimize its contribution to the total energy.

Although the insertion is localized to a few mesh points, it drives the local region of the surface to bulge and deform to minimize the energy after the insertion, and thus requires integration over the 3D surface to evaluate energy changes (Methods). To study the curvature sensing effect, we ran simulations on vesicles with five different radii: R = 7 nm, 14 nm, 28 nm, 56 nm, 112 nm respectively, as shown in Fig. 1E. For comparison with experimental data, we also used vesicles with R = 10 nm, and we studied cylinders of similar radii, as described in Methods. The curvature is defined as the inverse of the vesicle radius, so the initial vesicles have curvature in a range of 0.009–0.14 nm^{-1}, which covers a range of relevant membrane curvatures in biological systems.

Modeling helix insertion

The spontaneous curvature of bilayers is dependent on the lipid composition. For the vesicles studied here, we primarily assume the leaflets are symmetric, thus having a spontaneous curvature of zero, meaning the membrane prefers to be everywhere flat. We test in the Results how an initial asymmetry in the bilayer leaflets, producing a nonzero bilayer spontaneous curvature, would impact curvature sensing. The insertion of the oblong α-helix into a leaflet of the bilayer will induce conformational changes of nearby lipids. We therefore model the effect of the insertion as a local change to the spontaneous curvature of the membrane.[24] The area of this local change is chosen to mimic the size of the α-helix domain, which for ENTH occupies about

2 nm^2, *i.e.* 1 nm in width and 2 nm in length, on the membrane.[7,35] We thus select 4 triangles of the mesh to assign a nonzero value of c_0, which we will refer to as c_0^{ins} (Fig. 1C). In the Results we verify that the conclusions are unchanged with either higher mesh resolution, or with a more diffuse spreading of the local change in c_0^{ins}. The rest of the membrane surface retains the initial bilayer spontaneous curvature, usually zero. Optimized structures thus can form a bulge around the insertion (Fig. 1D). In this paper, we focus on the impact of one protein binding to the membrane, effectively assuming each binding event is local and independent of one another.

Comparison to experimental observables

The experimentally measured coverage of ENTH proteins per vesicle of radius R is reported in ref. 12, along with the experimental methods. We compute the corresponding K_{D} *via* $K_{\mathrm{D}} = [\mathrm{P}]^{\mathrm{eq}}\rho_{\mathrm{l}}^{\mathrm{eq}}/\rho_{\mathrm{el}}^{\mathrm{eq}}$, where $[\mathrm{P}]^{\mathrm{eq}}$ is the concentration of free ENTH in solution, $\rho_{\mathrm{l}}^{\mathrm{eq}}$ is the free lipid density on the surface, and $\rho_{\mathrm{el}}^{\mathrm{eq}}$ is the density of membrane-bound ENTH proteins. We exploit that both the proteins and the lipid sites are in great excess to the number of bound complexes, such that $[\mathrm{P}]^{\mathrm{eq}} = [\mathrm{P}]_{\mathrm{tot}}$ (150 nM) and $\rho_{\mathrm{l}}^{\mathrm{eq}} = \rho_{\mathrm{l}}^{\mathrm{tot}}$. The lipid binding-site density is calculated from the 7.5% mol fraction of lipids that are PI(4,5)P$_2$, as 0.125 nm^{-2} on all vesicles. The bound protein densities vary from 0.0038 to 0.0002 nm^{-2}. This K_{D} is thus dependent on radius (Fig. 1A), and the energetics of binding of one ENTH to the membrane surface can be extracted *via* the well-known relation

$$K_{\mathrm{D}}(R) = [1\mathrm{M}] \cdot \exp\left[\frac{\Delta G(R)}{k_{\mathrm{B}}T}\right], \tag{2}$$

where ΔG is the binding free energy and [1M] is the standard state concentration. Specifically, ΔG quantifies the free energy difference between (1) an unbound ENTH and the unperturbed membrane surface and (2) a bound ENTH to a perturbed membrane. For binding of ENTH domains with the helix removed, the K_{D} becomes effectively independent of radius, indicating that the enthalpic and entropic contributions due to binding the ENTH domain (minus helix) to the membrane do not change with membrane curvature (Fig. S1, ESI†).

While the binding free energy is clearly dependent on membrane curvature (Fig. 1), we decompose it into contributions that do not all vary with curvature. We emphasize that our calculations are not able to measure the binding free energy (eqn (2)), because we do not account for all chemical contributions to binding energy. Instead, our calculations measure the energy change upon binding that varies with curvature, due to membrane mechanics. We distinguish three contributions: a chemical potential due to electrostatic interactions between protein and lipids ($-\mu$), the cost of protein conformational change like the α-helix folding (ε), and a mechanical energy due to helix insertion into the bilayer (E). Without the helix, the ENTH domain still binds the membrane, but the binding is insensitive to curvature (Fig. S1, ESI†), hence we treat $-\mu$ as curvature independent. We will assume that the protein conformational change ε is also not dependent on the curvature given that the structure of the ENTH N-terminal α-helix is the same despite the different size of vesicles. Thus, $\Delta G(R) = -\mu + \varepsilon + \Delta E(R)$ and inserting this into eqn (2), we can write

$$\Delta E(R) = k_{\mathrm{B}}T \cdot \log\left[\frac{K_{\mathrm{D}}(R)}{K_{\mathrm{D0}}}\right], \tag{3}$$

where K_{D0} is independent of the membrane shape, $K_{\mathrm{D0}} = [1\mathrm{M}] \cdot \exp\left[\frac{-\mu+\varepsilon}{k_{\mathrm{B}}T}\right]$. To compare with simulations, we measure how these mechanical energies change relative to that of the smallest vesicle (E_{ref}), defining:

$$\Delta\Delta E(R) = \Delta E(R) - \Delta E_{\mathrm{ref}} = k_{\mathrm{B}}T \cdot \log\left[\frac{K_{\mathrm{D}}(R)}{K_{\mathrm{D}}(R_{\mathrm{min}})}\right], \tag{4}$$

where R_{min} = 10 nm (Fig. 1B). When the proteins and lipid binding sites are in excess of the membrane bound proteins (true here), this expression is independent of $[P]_{\mathrm{tot}}$ and $\rho_{\mathrm{l}}^{\mathrm{tot}}$. $\Delta\Delta E(R) = k_{\mathrm{B}}T \cdot \log\left[\frac{N(R_{\mathrm{min}})R^2}{N(R)R_{\mathrm{min}}{}^2}\right]$, where N is the copies of membrane bound proteins per vesicle of size R.

III. Results

IIIA. Spontaneous curvature of the insertion drives opposite changes in energy in small *vs.* large vesicles

The impact of our helix insertion on the membrane energy is controlled by its size, A_{ins}, (2 nm^2 unless otherwise noted) and by its spontaneous curvature, c_0^{ins}. For $c_0^{\mathrm{ins}} = 0$, the insertion would not change the membrane energy at all for any vesicle size, which we measure *via*

$$\Delta E = E_{\mathrm{bound}} - E_0, \tag{5}$$

where E_{bound} is the membrane energy with one helix bound and $E_0 = 8\pi\kappa$[34] is the energy of the spherical vesicle with no insertions and a surface spontaneous curvature $c_0(\boldsymbol{s})$ that is everywhere zero. This unperturbed energy E_0 results from the cost of bending the membrane into a sphere, when it prefers a flat curvature (c_0 across the unperturbed surface is zero), and is independent of vesicle radius.

As we increase c_0^{ins} of the insertion from 0.01 nm^{-1} to 0.3 nm^{-1}, we find that for smaller vesicles, the insertion lowers the cost of bending the membrane, producing $\Delta E < 0$ (Fig. 2A). For these highly curved vesicles, the insertion thus improves the stability of the bound system. Conversely, for larger vesicles, we see the opposite effect. Once $R > 28$ nm, insertions with increasing c_0^{ins} cause an increase in the cost of bending the membrane ($\Delta E > 0$), thus de-stabilizing these flatter surfaces.

These inverse costs and benefits of adding the insertion result from the initial strain that the membranes are under by being forced into curved (instead of flat) enclosed vesicles. For the highly curved small vesicles, the local mean curvature $H(\boldsymbol{s})$ is high and introducing an insertion that prefers higher curvature relieves strain in the membrane, even as it drives local shape changes. With larger vesicles, the local mean curvature $H(\boldsymbol{s})$ decreases, and the creation of local shape changes around the insertion eventually costs energy. The transition occurs at

 This journal is © The Royal Society of Chemistry 2021

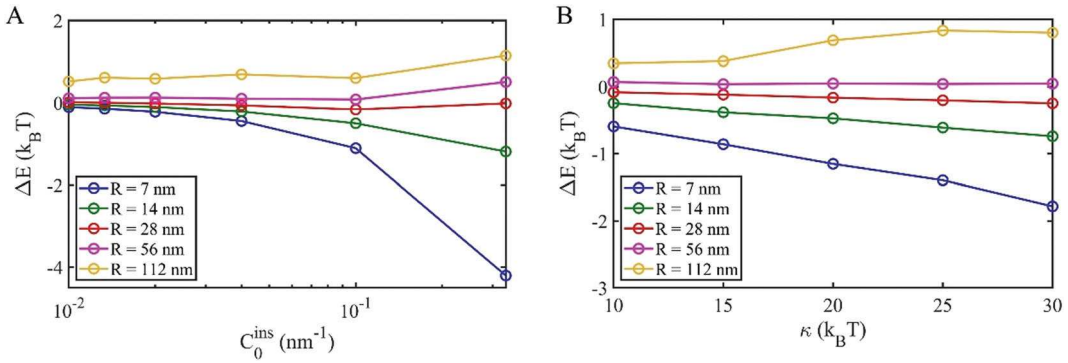

Fig. 2 The addition of insertions to spherical vesicles can stabilize or de-stabilize the bending energy dependent on vesicle size and bending modulus. (A) As c_0^{ins} increases, the insertion has a larger impact on the membrane energy, stabilizing small vesicles and de-stabilizing large ones. $\kappa = 20k_BT$. (B) As the bending modulus κ increases, the insertion is again more stabilizing for small vesicles, but de-stabilizing for large vesicles. $c_0^{ins} = 0.1$ nm^{-1}. The plotted energy change is due solely to the membrane mechanics, and is not the same as the binding free energy defined in eqn (2).

$\sim R = 28$ nm, where the corresponding membrane curvature is about 0.036 nm^{-1}. The transition between the positive and negative energy responses cannot be predicted from the vesicle size and insertion spontaneous curvature alone, as it depends on the relaxation of the surface around the insertion, as described further in Section IIIJ.

IIIB. Stiffer membranes also show opposite response to insertion in small *vs.* large vesicles

The response of the membrane energy to changes in bending modulus κ is also coupled with the vesicle size. For small curved vesicles, as we stiffen the membrane against bending (larger κ) the insertion produces a greater benefit in stabilizing the membrane (Fig. 2B), retaining a $\Delta E < 0$ and $d\Delta E/d\kappa < 0$. This result is again in agreement with the insertion relieving the strain in the membrane, which increases in the unperturbed vesicle with larger κ. For intermediate vesicles, the energy change becomes less sensitive to changes in κ, until we reach $R = 112$ nm. Now we see the opposite trend, where the increasing stiffness causes a larger cost to adding the insertion, producing $d\Delta E/d\kappa > 0$. The sign of ΔE does not change with κ, only the magnitude, as we quantify in Section IIIJ. However, we note that in Fig. 2B, the spontaneous curvature of the insertion zone is fixed at $c_0^{ins} = 0.1$ nm^{-1} for each data point, which means we effectively assume that the insertion (*e.g.* the insertion depth) is not influenced by the stiffness of the membrane. In reality, the insertion parameters of a specific α-helix type could be coupled to the membrane stiffness. So, given a specific helical structure, the response of the membrane energy to varying bending modulus κ could reflect simultaneous changes in both κ and c_0^{ins}. A relationship between κ and c_0^{ins} would depend on molecular properties of the protein–lipid interactions, and is beyond the scope of this paper.

IIIC. Area and volume changes have minimal impact on curvature sensing

The membrane energy is dependent on changes in volume and surface area due to insertion (eqn (1)), although we find they make negligible contributions relative to the bending energy. The volume constraint reflects an influence of osmotic pressure, where water may pass in and out of the vesicle to change its volume. The coefficient μ_V controls the penalty to changes in volume, and we find that over a broad range of values, it has minimal impact on the membrane energy after insertion (Fig. S2, ESI†). Similarly, the expansion or compression of the membrane area upon insertion is controlled by the coefficient μ_A, where experiments estimate this membrane elastic modulus in the range of 230–260 pN nm^{-1}.[36] Here again, over a broad range of values of μ_A, we see minimal changes to the membrane energy, indicating that global area changes upon insertion are not significant contributors to curvature sensing (Fig. S2, ESI†). In all of our simulations (unless otherwise noted), we thus use fixed values of $\mu_V = 83.4$ pN nm^{-2} and $\mu_A = 250$ pN nm^{-1}. The fact that these terms do not contribute to curvature sensing does not mean that they do not contribute at all to the binding free energy (eqn (2)), but only that the contribution is not sensitive to changes in curvature.

IIID. Helix insertion energies are sensitive to local curvature, not membrane surface area

Our results above show that the effect of the insertion on membrane energy is sensitive to the curvature of the membrane surface, as coupled to changing vesicle size. For a helix insertion with a fixed value of c_0^{ins}, we can thus see that as the vesicle gets smaller and more curved, the insertion drives more stable energies ($d\Delta E/dR > 0$), with a steeper benefit occurring for larger values of c_0^{ins} (Fig. 3A). For vesicles, both the curvature and the total membrane surface area change with varying vesicle radius, and on small vesicles the perturbation due to the insertion occupies a larger fraction of the total area than for larger vesicles. Therefore, we further tested whether curvature sensing would be retained when the surface area is fixed, and only the local curvature varies. We thus generated a single enclosed red-blood-cell-shaped membrane (by decreasing the vesicle volume[37]) that exhibits variations of curvature across its surface. Four different points with different curvatures on the surface were selected as the insertion zone (Fig. 3B). Our simulation results recapitulate the same curvature sensing

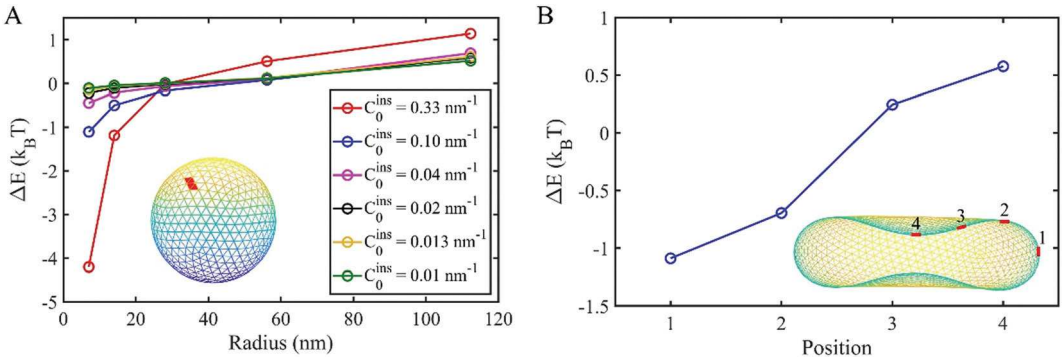

Fig. 3 Helix insertions will drive stronger binding to more highly curved membranes. (A) Curvature sensing on spherical vesicles. Inset illustrates a sphere of R = 7 nm along with the insertion area (red color). Insertions increase the stability of the membrane energy ($\Delta E < 0$) more robustly with smaller radius and correspondingly higher curvature ($1/R$). The magnitude of this response is larger with higher spontaneous curvature of the insertion c_0^{ins}. $\kappa = 20k_BT$. (B) Curvature sensing on an enclosed, red-blood cell shaped 'vesicle' with heterogeneous curvatures. Inset illustrates the side view with position 1 having highest curvature, and 4 having lowest (negative in this case) curvature. To get this asymmetric oblate structure, we started with the spherical vesicle R = 14 nm and set the target volume $V_0 = 0.65 \times 4\pi R^3/3$, target area $S_0 = 4\pi R^2$. A much stronger area and volume constraints were added with $\mu_V = 8.34 \times 10^4$ pN nm^{-2} and $\mu_A = 2.50 \times 10^4$ pN nm^{-1}. $\kappa = 20k_BT$ and $c_0^{\mathrm{ins}} = 0.1$ nm^{-1}. The membrane curvature at the positions labeled 1, 2, 3, 4 is 0.14, 0.08, 0.06, -0.06 nm^{-1} respectively. The membrane energy change ΔE is more stabilizing with higher curvature.

phenomena, where binding to the most highly curved region produces the largest benefit in membrane energy changes, and binding to regions of negative curvature produces a cost in membrane energy (Fig. 3B). The curvature sensing ability is thus robustly driven by the local curvature and resulting deformation around the insertion, rather than the relative size of the perturbation to the total surface area.

IIIE. Curvature sensing is retained when the insertion area is spread out

In the above models, the spontaneous curvature of the membrane at the site of the insertion is non-zero over an area of 2 nm^2, and immediately drops back to zero in adjacent surface elements. To test the effect of having a more continuous drop-off in spontaneous curvature as a function of distance from the helix, driven by a stressed distribution of lipids around the insertion,[20] we expanded the region of non-zero spontaneous curvature around the insertion (Fig. S3A, ESI†). The value of c_0^{ins} is thus largest at the center of the insertion, and decays with distance away. We model this decay using a Gaussian function:

$$c_0^{\mathrm{ins}}(x) = c_0^{\mathrm{ins}} \exp\left[-\frac{(x-x_0)^2}{2\sigma^2}\right], \quad (6)$$

where x is the distance to the insertion zone center x_0, and σ is the width of the spread. A Gaussian function introduces only one extra parameter in σ and concentrates most of the perturbation directly around the helix. The induced stress or strain is limited to $\sim$1 nm scale around the insertion,[20] so we choose $2\sigma \leq 1.5$ nm. We find that the curvature sensing effect is robustly retained, with a larger spreading of the insertion producing a larger change in the membrane energy (Fig. S3B, ESI†). Using a linear instead of a Gaussian function for the decay produces similar results (Fig. S3C and D, ESI†).

IIIF. The model recapitulates *in vitro* measurements of curvature sensing on vesicles of varying size

To most directly compare the simulation results to the experimental results of ENTH binding to vesicles,[12] we measure the energy change upon insertion relative to the value in the smallest vesicle ($\Delta E_{\mathrm{ref}}(R = 10$ nm)), so following eqn (4),

$$\Delta\Delta E(R) = \Delta E(R) - \Delta E_{\mathrm{ref}}. \quad (7)$$

We see excellent agreement between the shape of the energetic changes between both our numerical results and the experiment (Fig. 4), where in fact more than one set of κ–c_0^{ins} values agree quantitatively with the experiment. Hence, within physically reasonable values of the membrane bending moduli, a softer membrane reproduces the data with a larger spontaneous curvature ($c_0^{\mathrm{ins}} = 0.4$ nm^{-1}, $\kappa = 15k_BT$) or a stiffer membrane matches with a weaker spontaneous curvature ($c_0^{\mathrm{ins}} = 0.2$ nm^{-1}, $\kappa = 30k_BT$). We can see then that if the spontaneous curvature is either too large or too small, then the numerical results cannot reproduce observed bending energy changes for reasonable value of κ.

So far, we have assumed the spontaneous curvature across the bilayer surface is zero, $c_0(\boldsymbol{s}) = 0$, except at the insertion patch where $c_0^{\mathrm{ins}} > 0$. This will be true if both monolayers are symmetrical and identical in lipid composition, and thus we tested the role of a nonzero initial curvature driven by leaflet asymmetries. The simulation results show that curvature sensing persists and remains in close agreement with the experimental data (Fig. 5). Here we note that calculation of ΔE (eqn (5)) requires that E_0 also be calculated numerically, as it can deviate from the perfect sphere value of $E_0 = 8\pi\kappa$. Leaflet asymmetries can arise during the generation of vesicles, as specific lipids could prefer the inner leaflet over the outer leaflet due to the opposing curvature experienced by the head groups. For the vesicles used in the experiments, the composition is mainly DOPC ($\sim$90% of total lipids). DOPC has a

 This journal is © The Royal Society of Chemistry 2021

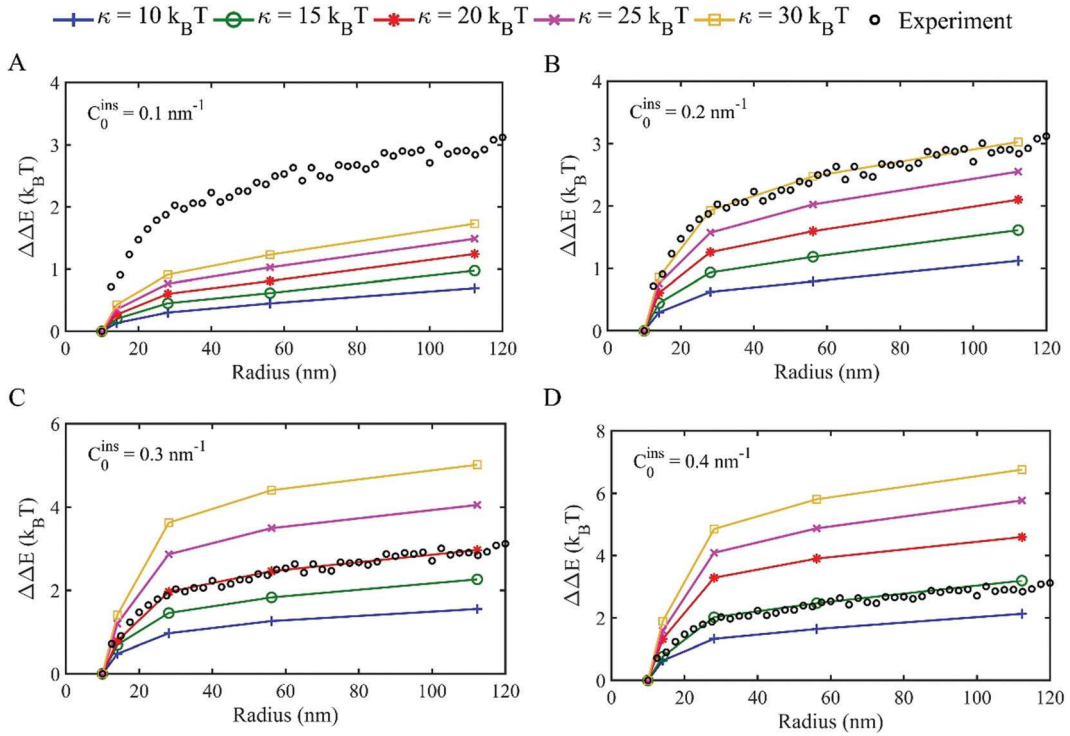

Fig. 4 Numerical simulations reproduce *in vitro* curvature sensing results of ENTH for realistic bending moduli and spontaneous curvature values. In all panels, the experimental data on binding to vesicles of varying radii is shown in black open circles,[12] same as in Fig. 1B (note the *y*-axis range varies with each panel). (A) For a lower spontaneous curvature (c_0^{ins} = 0.1 nm^{-1}), the curvature sensing is too weak to reproduce the experiment. (B–D) For values of c_0^{ins} = 0.2–0.4 nm^{-1}, we see excellent agreement with the experimental energetics, where the agreement is dependent on pairing of c_0^{ins} and κ.

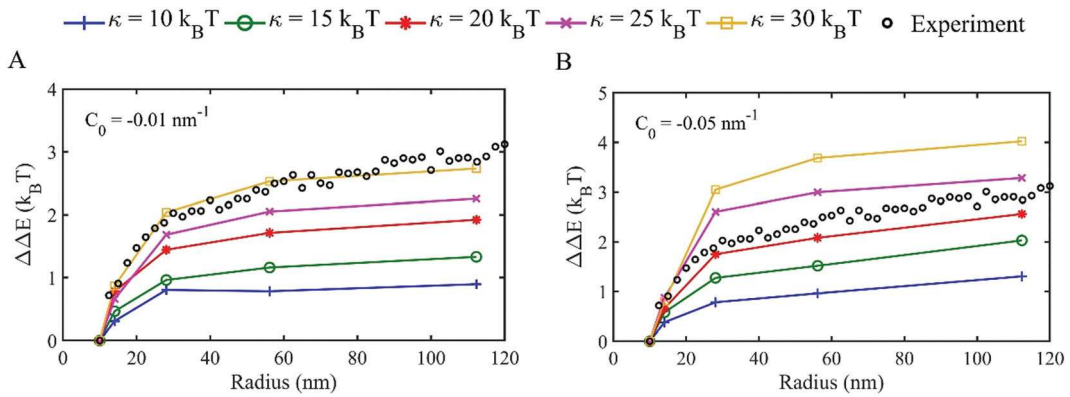

Fig. 5 Numerical simulations reproduce the *in vitro* curvature sensing on vesicles even when the bilayers initially have a nonzero spontaneous curvature. (A and B) In both panels, the experimental data is shown in black open circles and c_0^{ins} = 0.2 nm^{-1}. (A) The bilayer spontaneous curvature is initialized to $c_0(\boldsymbol{s})$ = −0.01 nm^{-1} to reflect possible asymmetries in the inner and outer leaflet. Results are very similar to the same model with $c_0(\boldsymbol{s})$ = 0 nm^{-1} shown in Fig. 4B. (B) With a more negative initial value, $c_0(\boldsymbol{s})$ = −0.05 nm^{-1}, the experimental data agrees better with a softer (lower κ) membrane given the same value of c_0^{ins}. Thus realistic values of κ–c_0^{ins} describe the experimental data even with initial asymmetries between membrane leaflets.

negative spontaneous curvature about −0.05 nm^{-1},[38] meaning that the spontaneous curvature of each monolayer is about −0.05 nm^{-1}. Because a nonzero *bilayer* spontaneous curvature is only caused by asymmetries between the monolayers, no matter their individual values, we thus tested bilayer values starting from a maximal asymmetry: $-0.05\ \text{nm}^{-1} \leq c_0(\boldsymbol{s}) \leq 0$. Overall, for small deviations from zero, the influence is negligible (compare Fig. 4B and 5A), while for the larger deviations we observe enhanced curvature sensing with the same insertion parameters (Fig. 5B).

IIIG. The model recapitulates *in vitro* measurements of curvature sensing of distinct amphipathic helices, ALPS1 and ALPS2

Our above results focused on the epsin N-terminal (ENTH) amphipathic helix, which is ∼2 nm^2 in area. The ArfGAP1

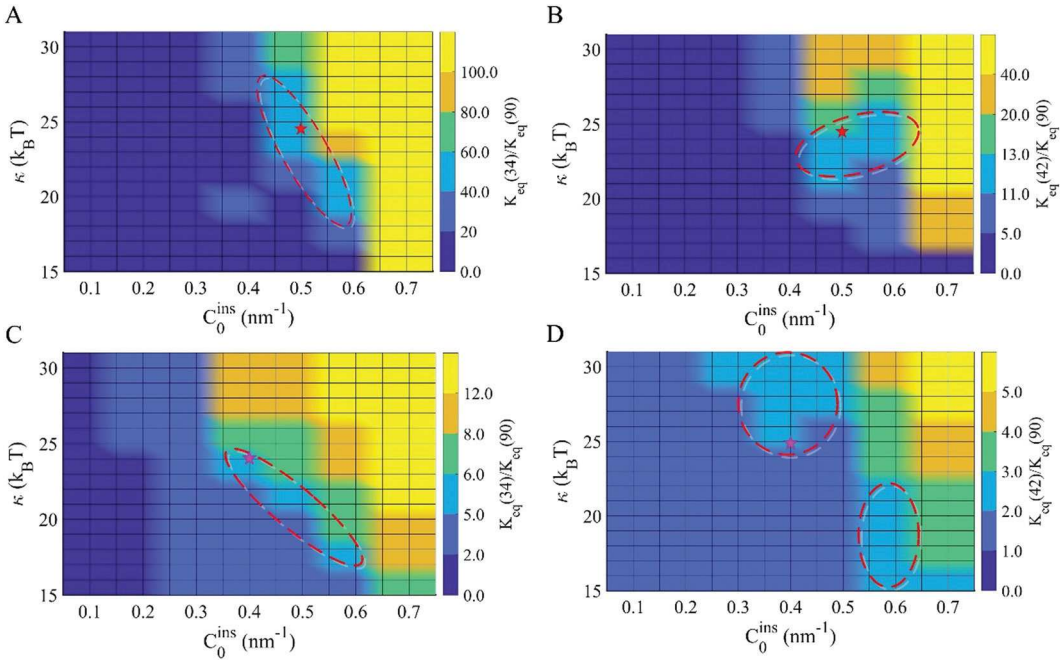

Fig. 6 Numerical simulations can reproduce the *in vitro* curvature sensing of the two ArfGAP1 ALPS helices. In all panels, the color bars indicate the increased binding observed on highly curved vesicles (R = 34 nm in A–C and R = 42 nm in B–D) relative to a reference vesicle of R = 90 nm. (A and B) Simulation results for the ALPS1 motif, with A_{ins} = 6 nm^2. The experimentally measured values are $K_{eq}(34)/K_{eq}(90)$ = 46.75, $K_{eq}(42)/K_{eq}(90)$ = 11.51.[13,16] Thus the red dashed circles represent the possible κ–c_0^{ins} pairs that reproduce this experimental data, with the red star indicating a conserved κ values across all 4 panels. (C and D) Simulation results for the ALPS2 motif, with A_{ins} = 3.5 nm^2. The experimentally measured values are $K_{eq}(34)/K_{eq}(90)$ = 5.33, $K_{eq}(42)/K_{eq}(90)$ = 2.25.[13,16] Thus the red dashed circles represent the possible κ–c_0^{ins} pairs that reproduce this experimental data, with the pink star indicating a conserved κ values across all 4 panels.

protein contains two slightly longer amphipathic helices, termed ALPS1 and ALPS2, that can also insert into membranes.[11] Both these helices have been shown experimentally to exhibit curvature sensing, with ALPS1 being a stronger sensor of curvature.[16] Based on structural data,[16] we therefore set the ALPS1 insertion area to 6 nm^2, and the ALPS2 insertion area to 3.5 nm^2. Our continuum model was again able to reproduce the experimentally measured curvature sensing for both these helices with realistic pairs of bending modulus κ and insertion spontaneous curvature c_0^{ins} (Fig. 6). Specifically, both helices were experimentally studied on vesicles of radii 90, 42, and 34 nm, with the same composition in each.[16] We therefore expect similar values of κ to describe sensing for both helices, and indeed for $\kappa = 24k_BT$, we found very good agreement for both helices using c_0^{ins} = 0.5 nm^{-1} for ALPS1, and c_0^{ins} = 0.4 nm^{-1} for ALPS2. Fig. 6 highlights other pairs of κ–c_0^{ins} with good agreement to the experiments.

IIIH. The model recapitulates *in vitro* measurements of curvature sensing by ENTH on cylinders of varying size

Curvature sensing of the ENTH domain was also experimentally observed on cylindrical membrane tethers of varying size by Capraro *et al.*[17] In Fig. 7, we show that our model produces good agreement with the experimental results. The optimal parameters for the model used the same A_{ins} = 2 nm^2 as the ENTH on the vesicles, with $\kappa = 20k_BT$ and c_0^{ins} = 0.45 nm^{-1}. This insertion spontaneous curvature is somewhat larger but still relatively similar to the value for ENTH used on the vesicles, where we found excellent agreement when $\kappa = 20k_BT$ and c_0^{ins} = 0.3 nm^{-1} (Fig. 4). One reason for a difference in c_0^{ins} for the same protein on cylinders *vs.* vesicles could be the different lipid compositions used in the two experiments. In addition, due to the change in geometry, specific proteins have been shown to sense curvature more strongly in vesicles over cylinders (although ENTH was not studied).[39] Our model does not assume that sensing need be identical in cylinders and vesicles of the same mean curvature. This is evident because the shape of the membrane deforms following insertion, and the exact shape and energetic cost of the deformation can be sensitive to the unperturbed surface topology. In Section IIIJ below we quantify how the shape deformation, on its own, impacts energetics as a function of vesicle size.

We note that to compare our measurements directly to the quantitative experiments (see Methods for all cylinder simulation details), the experimental results showed that the ratio of protein (I_p) and lipid (I_l) fluorescence intensities on the tether, $I_r = I_p/I_l$, is linear with the square root of tension on the tether, or equivalently, with the inverse of the tether radius R.[17] This normalized intensity ratio, I_r/I_r^0, where I_r^0 is the fluorescence intensity ratio of a reference cylinder, is the same as a normalized binding constant K_{eq}/K_{eq}^0, when, similar to the vesicle experiments, the abundance of unbound protein and of lipid binding sites are in excess and thus effectively constant across R. Using eqn (4), we quantify $K_{eq}/K_{eq}^0 = \exp(-\Delta\Delta E/k_BT)$ where $\Delta\Delta E = \Delta E(R) - \Delta E_{ref}$, as defined in eqn (7). Thus, by measuring the membrane energy change caused by inserting an amphipathic

 This journal is © The Royal Society of Chemistry 2021

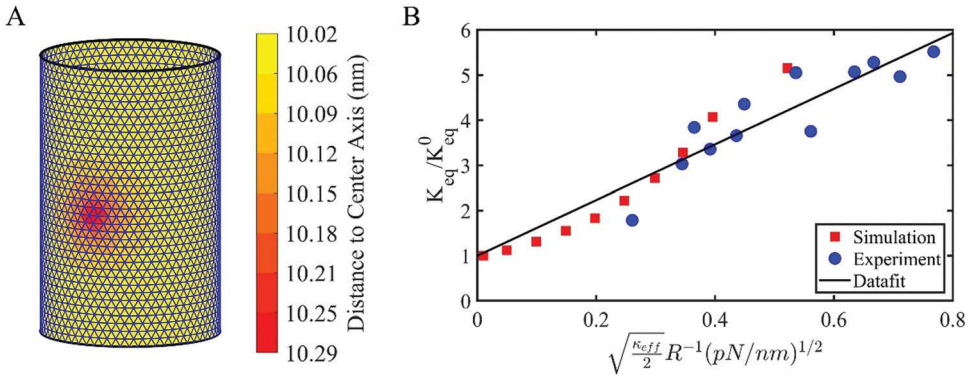

Fig. 7 Numerical simulations reproduce the *in vitro* curvature sensing results observed on cylindrical membrane tethers. (A) Modeled cylinder showing the local bulge that occurs following one insertion on the cylinder membrane. Here R = 10 nm, $\kappa = 20k_BT$, and c_0^{ins} = 0.3 nm^{-1}. The color bar shows the distance of each triangular face to the axis of the cylinder. All modeled cylinders have a length of 55.4 nm with both ends constrained by periodic boundary conditions, with this image zooming in on a length of L = 30 nm to highlight the bulge. (B) The experimental data measured increased binding on tethers as tension increased and their radii decreased (1/R increased), as plotted in Fig. 2E of ref.17 and $\kappa_{eff} = 13.33k_BT$ according to their system set-up. Our numerical simulations were carried out with $\kappa = 20k_BT$, c_0^{ins} = 0.45 nm^{-1}, and A_{ins} = 2 nm^2. $K^0_{eq} = K_{eq}(R$ = 500 nm). In Fig. S4 (ESI†), we plot the same data in (B) *vs.* R, to show the similar representation as our earlier figures.

helix on cylinders of decreasing radii down to R = 10 nm, our model recapitulates the experimentally observed curvature sensing (Fig. 7), with a similar dependence on R of ENTH on the spherical vesicles (Fig. S4, ESI†). We note that our model results are not as linear as the experimental data, and this could be due to our assumption that $I_r/I_r^0 = K_{eq}/K^0_{eq}$. Although the solution proteins are in clear excess of the bound proteins, the lipid sites are not strictly in excess. While unbound lipid binding sites could remain constant due to exchange between the tether membrane and the reservoir, this is difficult to verify, and a correction term would account for changes in unbound lipid populations with increasing K_{eq}. We do not attempt this here because the absolute values of K_{eq} are not known (*i.e.* our model does not report on enthalpic contributions to binding strength).

IIII. The model captures increased binding on membranes with lipid composition of increasingly negative spontaneous curvature

Lastly, we consider a set of experiments that showed how binding affinities for amphipathic helices could also vary across vesicles that have a fixed size but changing membrane composition.[13,33] We make two new assumptions for these model calculations, and emphasize that this renders this specific comparison less robust than previous results. Nevertheless, our model achieves good agreement with experiment (Fig. 8), and thus we consider the results at least qualitatively promising. The first key assumption is that the changing lipid composition does not affect the enthalpic or entropic contributions of the binding interaction. Instead, by keeping the percentages of negatively charged lipids constant, but increasing the fraction of the wedge-shaped diacylglycerol (DAG) lipid, both monolayers of the bilayer exhibit an increasingly negative spontaneous curvature, $c_0(\boldsymbol{s})$. This could therefore alter the membrane bending energy following insertion, and thus the binding affinity. Experiments showed that a truncated ArfGAP1 containing its ALPS1 helix has a higher affinity to vesicles with more DAG (see Fig. 7B in ref. 13). A second key assumption of our model is that we here use the continuum surface to represent only a monolayer of the membrane (the outer-leaflet of the vesicle), with the assumption that

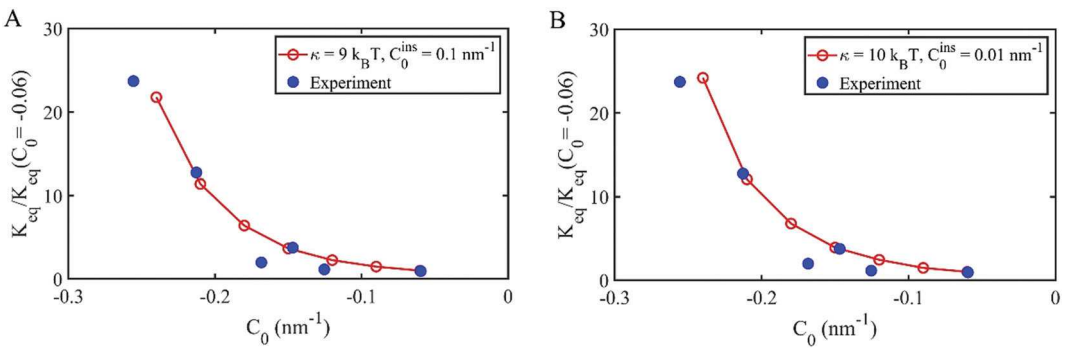

Fig. 8 Numerical simulations show stronger binding to membranes with a composition that has a more negative spontaneous curvature, similar to *in vitro* results The experimental data is shown in blue dots[13,33] in both plots, our numerical results in red circles. (A) With softer monolayer κ, a larger c_0^{ins} = 0.1 nm^{-1} agrees best. (B) With stiffer monolayer κ, a smaller c_0^{ins} = 0.01 nm^{-1} is needed. Simulations were run on a vesicle with R = 28 nm, consistent with the experiments. K_{eq}/K^0_{eq} is the normalized equilibrium constant that can be calculated from eqn (4) given $\Delta\Delta E = \Delta E - \Delta E_0$, and ΔE_0 is the energy change due to insertion on the reference membrane defined to have initial spontaneous curvature $c_0(\boldsymbol{s}) = -0.06$ nm^{-1} across the vesicle surface.

energetic coupling to the inner-leaflet is neglectable. It will be important to test and quantify this assumption in future work with a multi-leaflet continuum model (see Discussion), but here we simply show the results based on these assumptions. Therefore, our model has only one layer, with $\kappa = 9$–$10k_BT$ (the value for a monolayer), and we again measure ΔE due to one insertion as the initial spontaneous curvature of the membrane is made more negative. Similar to the experiment, we also find stronger binding to membranes with more DAG (a more negative $c_0(\mathbf{s})$), using $c_0^{ins} = 0.1$ nm^{-1} and $\kappa = 9k_BT$, or $c_0^{ins} = 0.01$ nm^{-1} and $\kappa = 10k_BT$ (Fig. 8). We use one insertion with $A_{ins} = 4$ nm^2, which was found to be optimal from numerical calculations performed using elasticity theory.[13]

IIIJ. Predictive model for membrane energy changes following insertion captures effect of membrane shape changes

To combine all of our numerical results into a simpler mathematical framework, we derived a phenomenological expression to predict how the membrane energy changes would vary with c_0^{ins}, κ, vesicle radius R, and insertion area A_{ins}. This expression clarifies how the observed energy change results not only from the local change in spontaneous curvature at the insertion (which can be calculated analytically), but the membrane shape changes that occur following membrane relaxation around the insertion. The results apply for initial bilayer spontaneous curvature of $c_0(\mathbf{s}) = 0$, or symmetric bilayers.

We write the total observed membrane energy change calculated from numerical simulation as

$$\Delta E(R, c_0^{ins}, \kappa, A_{ins}) = \Delta E_0 + \delta, \quad (8)$$

where ΔE_0 is the change in bending energy due solely to changes in spontaneous curvature at the insertion, without any shape change to the surface. Therefore, δ captures energy changes due to deformation of the membrane shape to relieve induced strain in the surface. We calculate ΔE_0 analytically using eqn (1). The only change in energy across the surface occurs at the site of the insertion. Before the insertion, the membrane bending energy of the area A_{ins} is $\frac{\kappa A_{ins}}{2}\left(\frac{2}{R}\right)^2$, with the spontaneous curvature of the membrane being zero. After the amphipathic helix inserts into this area A_{ins}, the bending energy on this area is $\frac{\kappa A_{ins}}{2}\left(\frac{2}{R} - c_0^{ins}\right)^2$ with c_0^{ins} being the

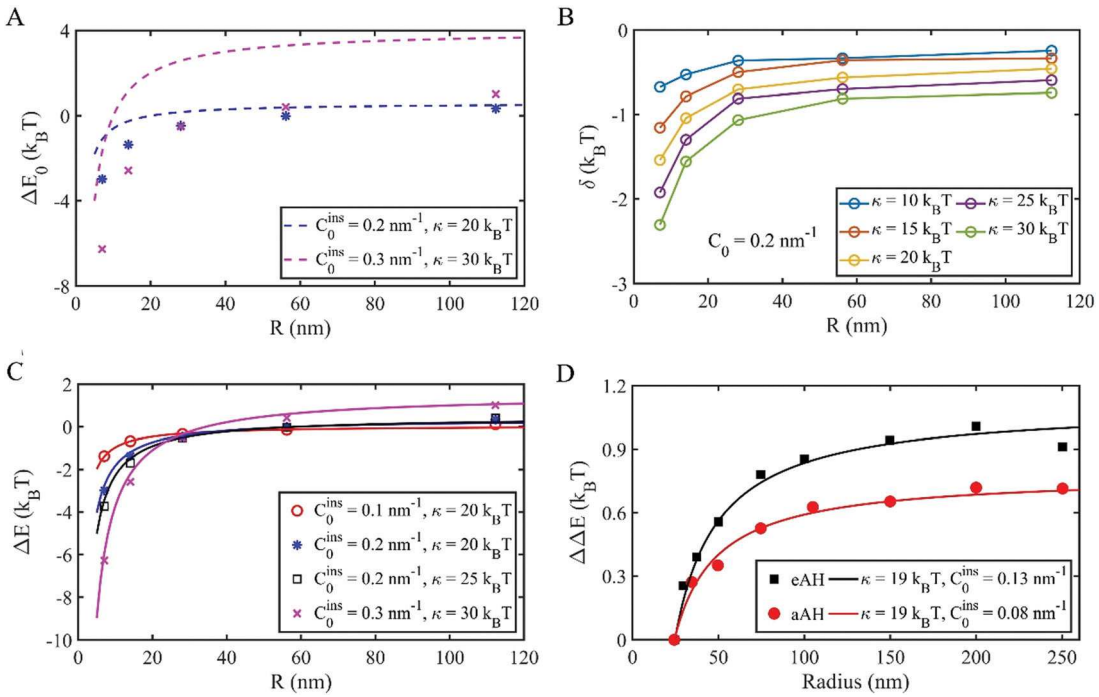

Fig. 9 Empirical formula predicts dependence of membrane energy change on physical parameters due to the insertion and subsequent membrane shape changes. (A) The dashed lines show ΔE_0, which is defined analytically in eqn (9) as the change in bending energy due solely to changes in spontaneous curvature at the insertion, without membrane shape relaxation. This simple estimate significantly overestimates the energy changes observed at equilibrium from our simulations (ΔE), which are shown in the blue and pink data points. These data points are the same as the matching color/symbol in part (C). (B) From our numerical simulations that produce ΔE, we can extract the energy change δ that arises only due to membrane shape relaxation using $\delta = \Delta E - \Delta E_0$, where ΔE_0 is defined analytically in eqn (9). (C) The total energy change ΔE is found from our numerical simulations (data points), as also shown in previous figures. ΔE arises due to both changes to the spontaneous curvature at the insertion, and subsequent membrane shape relaxation. Our empirical model derived in eqn (11) (solid curves) provides excellent agreement with the simulated results. (D) Application of eqn (11) to quantify experimental data of helix-containing eAH and aAH.[9] Based on this published study, we set $A_{ins} = 4$ nm^2 for eAH and $A_{ins} = 4.75$ nm^2 for aAH. $\Delta\Delta E = \Delta E(R) - \Delta E(R_0)$, where $\Delta E(R)$ is calculated by eqn (11) and $R_0 = 24.3$ nm.

This journal is © The Royal Society of Chemistry 2021

effective spontaneous curvature on this binding area A_{ins}. We thus have:

$$\Delta E_0(R, c_0^{ins}, \kappa, A_{ins}) = \frac{\kappa A_{ins}}{2}\left(\frac{2}{R} - c_0^{ins}\right)^2 - \frac{\kappa A_{ins}}{2}\left(\frac{2}{R}\right)^2 = \frac{\kappa A_{ins}}{2}\left(c_0^{ins^2} - \frac{4c_0^{ins}}{R}\right) \quad (9)$$

as the membrane energy change from one insertion before the relaxation of the stress or strain (Fig. 9A).

We use our numerical results to derive an expression for δ. Our results show δ is always a negative value (Fig. 9B), which means the relaxation process always causes the membrane energy to decrease, whereas ΔE_0 is positive when $c_0^{ins} > 4/R$. From our analysis, we find that δ varies with all four parameters, $\delta = \delta(R, c_0^{ins}, \kappa, A_{ins})$. The simulation results show $\delta \propto \kappa$ and that δ is a linear function of R^{-1} (Fig. S5, ESI†), which is the same dependence that ΔE_0 has (eqn (9)). For the insertion parameters, however, we find that δ has distinct scaling with c_0^{ins} and A_{ins}. Specifically, we find that $\delta / {c_0^{ins}}^{1.5}$ is independent of c_0^{ins}, and $\delta / {A_{ins}}^{1.25}$ is independent of A_{ins} (see Fig. S5, ESI† for details on parameter estimation). By fitting our numerical data, we thus recover a final practical expression for how δ depends on all four variables:

$$\delta(R, c_0^{ins}, \kappa, A_{ins}) = -\kappa {c_0^{ins}}^{1.5} A_{ins}^{1.25}\left(\frac{3}{2R} + \frac{1}{R_0}\right). \quad (10)$$

This expression contains 4 fit parameters: the exponents 1.5 and 1.25, the 3/2 prefactor for R^{-1}, and finally $R_0 = 10$ nm is a fit parameter necessary to capture the apparent plateauing of δ at negative values when $R \to \infty$.

By combining eqn (8)–(10), we have the final analytical expression of the membrane energy change due to one helix insertion as:

$$\Delta E(R, c_0^{ins}, \kappa, A_{ins}) = \frac{\kappa A_{ins}}{2}\left(c_0^{ins^2} - \frac{4c_0^{ins}}{R}\right) - \kappa {c_0^{ins}}^{1.5} A_{ins}^{1.25}\left(\frac{3}{2R} + \frac{1}{R_0}\right), \quad (11a)$$

or

$$\Delta E(R, c_0^{ins}, \kappa, A_{ins}) = \kappa A_{ins} c_0^{ins}\left[\frac{c_0^{ins}}{2} - \frac{2}{R} - \sqrt{c_0^{ins}} {A_{ins}}^{\frac{1}{4}}\left(\frac{3}{2R} + \frac{1}{R_0}\right)\right]. \quad (11b)$$

Eqn (11) provides excellent agreement with the numerical data as shown in Fig. 9C, recovering the proper limits that as the size or spontaneous curvature of the insertion goes to zero, there is no change in the membrane energy, as expected. This model further predicts when the helix insertion will cause stabilization ($\Delta E < 0$) or de-stabilization ($\Delta E > 0$) to the membrane energy, dependent on c_0^{ins}, R, and now also A_{ins}. The sign is thus independent of κ, as seen in Fig. 2B. This expression shows that the membrane energy changes for vesicles is most sensitive to changes in c_0^{ins}, which is coupled to the vesicle radius most strongly *via* the membrane shape changes, as seen in the last term of eqn (11a) $\left({c_0^{ins}}^{1.5}/R\right)$. The trend is similar for the insertion size, where it couples more strongly to the vesicle radius in the membrane shape changes (${A_{ins}}^{1.25}/R$). The magnitude of the energy change following relaxation is comparable to the energy change due to the insertion (Fig. S5E, ESI†), meaning that the contribution of the membrane shape changes in response to helix insertion cannot be ignored when quantifying the strength of helix localization to membranes.

As an example application of this formula, we used eqn (11) to fit experimental data of curvature sensing of two helices, eAH and aAH, on liposomes of varying radii (from Fig. 2E in ref. 9). Similar to all previous calculations, we re-plot the reported $\Delta G(R)$ values[9] by subtracting off $\Delta G(R_0)$, to directly compare with the analytically predicted $\Delta E(R) - \Delta E(R_0)$, with R_0 = 24.3 nm, the smallest vesicle in their experiments. The best fit of the data to eqn (11) is in excellent agreement, and is in the expected parameter ranges, with $\kappa = 19 k_B T$ and $c_0^{ins} = 0.08$ and 0.13 nm^{-1} for aAH and eAH (Fig. 9D).

IV. Discussion

Curvature sensing by amphipathic helices emerges from their localized disruption of, primarily, the leaflet of the bilayer where they embed. The energy change that results from this localized perturbation is up to a few $k_B T$, based on experimental measurements. We show here that curvature sensing by amphipathic helices and the corresponding energy changes can be accurately captured by deformable continuum membrane models, despite lacking an explicit double leaflet structure. Instead, the spontaneous curvature of an insertion area, which is a material property reflective of stresses induced on only one leaflet, can effectively couple inserted helices to the membrane bending energy. Our numerical results predict stronger binding of helices to membranes of higher curvature. The form of the curvature-dependent binding energy (not the complete binding free energy which is not accessible with this model) is in excellent quantitative agreement to experiments. Furthermore, using literature standard values for κ (15–20$k_B T$),[40] and predicted values for c_0^{ins} (0.1–0.5 nm^{-1}),[22] the experimental observations are directly within the range of reasonable parameters. The energy change that accompanies helix insertion is due to the bending energy, and we decompose this energy change into two parts: the cost of the helix insertion (change in c_0^{ins}) and the energy of the shape change following insertion. Both components make comparable contributions to the overall change in bending energy. We develop an empirical formula that can then predict these energy changes, which quite accurately captures dependence on the bending modulus, sphere radius, helix insertion size, and insertion spontaneous curvature. We can therefore predict when helix insertion acts to relieve stress in the membrane (highly curved vesicles) or introduce new strain (low curved vesicles). We verify that the observed energy changes are due to sensing of the local curvature around the insertion, as the result is retained in non-spherical surfaces of constant surface area, and as the helix insertion is spread.

We assume the binding of each amphipathic helix is independent of each other. This applies for the low concentrations used in the experiments here, where the density of ENTH on the vesicle membrane surface never surpassed 0.0038 nm^{-2} (<5% surface coverage-Fig. S6, ESI†) and no clustering of proteins was observed.[12] For the experiments with ALPS motifs[16] and ENTH on cylinders,[17] we estimate similarly low surface coverage of at most 4% and 12%, respectively (see Methods). However, at higher densities, the local shape changes could alter the binding energetics of subsequent proteins, leading to mechanically induced feedback. The shape and energetics of the deformation can vary as protein pairs move closer together,[41] and mechanical feedback can alter rates of binding to membranes.[42] The spatial distribution or interactions between proteins on the membrane can also vary due to localized changes to bending energy and membrane shape.[31] At coverage above 20%, additional curvature induction mechanisms such as crowding,[7] would enhance shape changes beyond helix insertion alone. The modeling approach used here is capable of quantifying even small changes in energy that could emerge due to cooperative effects. In future work we will address how feedback and cooperativity can drive enhanced or depressed recruitment to surfaces of varying curvature.

A limitation of the thin-film surface model is that it does not explicitly capture the thickness of the bilayer or any explicit asymmetry between inner and outer leaflets. The model thus cannot quantify how the stress profile in the membrane varies[13] from the embedded leaflet, where the helix causes stretching, relative to the presumably more compressed opposite leaflet. Initial asymmetries between leaflets prior to insertion also influences the initial bilayer spontaneous curvature, although we showed here that curvature sensing persists even when $c_0(\boldsymbol{s}) \neq 0$, causing minimal changes to bending energies as it approaches zero (Fig. S7, ESI†). However, explicitly capturing each monolayer leaflet would be important for more accurately testing how changes to lipid composition[33] would impact bending energies (see Section IIII), including more directly accounting for lipid-packing defects that influence monolayer spontaneous curvature.[11] Where finer-grained detail is required, applications of material-elastic theory[13] to membrane patches thus have an advantage in this regard, although they have significantly less flexibility in studying topological variations of surfaces that exist in three-dimensions. Our approach here benefits from previous material-elastic studies that have predicted ranges of c_0^{ins} from helix shape and mechanical strain.[20,22] Furthermore, membrane thickness has been shown to be an important variable for interactions between fully transmembrane proteins that span both leaflets.[20,22] Studying the role of membrane thickness in continuum models can be achieved through coupling of two layers together, and hybrid methods that combine continuum membranes with atomistic proteins capture realistic deformations around transmembrane proteins.[31,43] Coupling the two layers would introduce an energy term due to thickness changes (typically modeled harmonically), and could also include energetics of lipid tilt. Similar to the area and volume constraints, we anticipate that these terms will be relatively small compared with the bending energy cost, and thus would not significantly shift our energetic measurements for curvature sensing by a single helix. Here, we found that capturing explicit membrane thickness was not necessary to reproduce experiment, as the spontaneous curvature accurately quantified helix-induced membrane strain on vesicles and cylinders.

Overall, the modeling approach used here offers an accurate, experimentally verified platform to study membrane shape changes and bending energies arising from adsorbed proteins, despite relatively few free parameters. To quantify curvature sensing by amphipathic helices, we found it to be efficient across multiple changes to material properties of the membrane and the insertion, even over $\sim k_{\mathrm{B}}T$ or smaller energy changes. The direct comparison between quantitative experiments and modeling provides a mechanism to determine coarse material parameters of proteins, where here we found that inserted helices have a spontaneous curvature of 0.1–0.4 nm^{-1}, using realistic membrane bending moduli. Modeling membranes at the mesoscale has proved critical for studying key steps in processes from clathrin-mediated endocytosis,[44] to fluctuations in red-blood cell membranes,[45] where molecular approaches are simply intractable. By further coupling mesoscale membranes to dynamical protein systems using, for example, reaction-diffusion methods,[46] the time-evolution of surface shape driven by multiple interacting proteins could also be captured in addition to energetics. Our code is therefore provided open-source under a Gnu Public Licence (GPL) at github.com/mjohn218/NERDSS/continuum_membrane. Given the breadth of membrane bending processes that occur in the cell,[47] this mesoscale approach can be usefully applied and extended to quantifying key mechanisms of protein-driven membrane remodeling.

V. Methods

VA Set-up of vesicles

An enclosed spherical triangular mesh is set up by the Loop's subdivision scheme at the radius of interest.[48] The limited surface area is calculated as the vesicle area S, and the volume enclosed by the vesicle area is calculated as the vesicle volume V.

VB Energy minimization

The equilibrium state of the vesicle is produced by minimizing the total energy using nonlinear conjugate gradient methods (NCG).[49] The force on each vertex is expressed as the derivative of the total energy to the vertex position

$$\vec{f}_i = -\frac{\partial E}{\partial \vec{x}_i}, \tag{12}$$

where $\vec{x}_i$ and $\vec{f}_i$ are the position and nodal force on vertex i respectively, and the detailed expression can be found in.[23,37] The total energy includes terms due to the regularization and area constraint on the insertion described below. As criteria for stopping the minimization (finding the optimum), we use a

 This journal is © The Royal Society of Chemistry 2021

mean nodal force is smaller than 10^{-2} pN and that the energy curve slope is $(E_{i+500} - E_i)/500 < 10^{-3}$ (E_i is the total energy in simulation step i), as shown in Fig. S8 (ESI†).

The calculation time depends on the vesicle size. The larger vesicle has more triangular faces and vertices, requiring more time to finish the energy minimization. For the small vesicle (R = 10 nm), each minimization takes 5–30 minutes on 48 cores, with the code written in c++ using OpenMP threading. Minimization takes longer with larger values of c_0^{ins}. For the large vesicle (R = 120 nm), the same calculation takes about 2–4 days.

VC Insertion area constraint

We constrain the area of the insertion zone, as the nonzero c_0^{ins} makes the triangular mesh nonuniform around the insertion, and we do not want the mesh deformation to change the area of the insertion (which is typically fixed at 2 nm^2 for ENTH insertion). Therefore, we tried two methods which produce very similar results, and neither of which measurably impacts the total energy of the system, which is dominated by the bending energy (Fig. S9, ESI†). Using an edge length energy we have:

$$E_{\text{insertion}} = \sum_i \frac{1}{2} K \left(l_i - l^0\right)^2, \tag{13a}$$

where l_i is the edge length of the insertion zone, $l^0 = \sqrt{2/\sqrt{3}}$ nm is the targeted length for the insertion zone, and K is the spring coefficient. The sum of eqn (13a) covers all the edges of the insertion zone. Alternatively, the insertion area can be constrained *via* a local area constraint:

$$E_{\text{insertion}} = \sum_{i=1}^{4} \frac{1}{2} \mu_{\text{A}} \frac{(A_i - A_0)^2}{A_0}, \tag{13b}$$

where A_i is the area of one triangle in the insertion zone, A_0 = 0.5 nm^2 is the target area of the insertion zone triangle (the total area of the insertion zone is 2 nm^2, and the insertion zone has four triangles so each triangle should have area 0.5 nm^2), and μ_{A} is the membrane area elasticity modulus as in eqn (1). To use eqn (13b) for the insertion area constraint, we need to separate out the insertion area from the global area constraint in eqn (1).

VD Evaluation of surface integrals

The numerical solution of the integral over the surface in this theoretical model (eqn (1)) is calculated by second order Gauss-quadrature. We validate that the second order of Gauss-quadrature is sufficient to produce converged energy estimates, and the higher-order and more expensive quadrature schemes are not necessary (Fig. S10, ESI†). We also validate that the fineness of the triangular mesh doesn't influence the energy calculation (Fig. S11, ESI†), verifying that the resolution used here is sufficient to accurately measure energy changes following insertion.

VE Regularization energy

To eliminate the in-plane shearing deformations of the triangular mesh, we add a regularization energy.[37] The regularization energy has two forms depending on whether the triangular element is too biased from the equilateral shape. The function to describe the shape of triangular element i is defined by

$$\eta_i = \sum_{j=1}^{3} \left(l_{i,j}/\bar{l}_i - 1\right)^2, \tag{14}$$

where $l_{i,j}$ is the edge length and $\bar{l}_i = \sqrt{4A_i/\sqrt{3}}$ is the target edge length with A_i being the triangular element area. A large η_i means the triangle is more deformed, and here in our simulations we use η_0 = 0.2 as the criteria determining whether the triangle shape is too deformed. If $\eta_i > \eta_0$, the regularization energy for this triangular element i is

$$E_{\text{reg},i} = \sum_{j=1}^{3} \frac{1}{2} k \left(l_{i,j} - \bar{l}_i\right)^2, \tag{15a}$$

where k is the coefficient of this spring-type energy. If $\eta_i \le \eta_0$, the regularization energy for this triangular element i is

$$E_{\text{reg},i} = \sum_{j=1}^{3} \frac{1}{2} k \left(l_{i,j} - l_{i,j}^0\right)^2, \tag{15b}$$

where $l_{i,j}^0$ is the edge length we choose to use which is called the reference structure. Then the total regularization energy is the sum of all the N triangular elements of the mesh.

$$E_{\text{reg}} = \sum_{i=1}^{N} E_{\text{reg},i}. \tag{16}$$

The regularization energy controls sizes of mesh elements which improves numerical integration over the surface, and thus is a technical constraint on the numerical method rather than physical constraint on the membrane energy, so it should converge to 0 when the system reaches the equilibrium state. The reference structure (value of $l_{i,j}^0$) needs to be updated as the simulation evolves, and we update it when the energy optimization slows. This update method ensures that eqn (16) will converge to 0 and that the regularization works effectively on remeshing the triangular mesh.[37] Note that eqn (15) is not a continuous function, so it may cause a problem to find an efficient step size during the NCG energy minimization, but practically this problem can be solved by restarting the simulation or by shutting down eqn (15a) for several simulation steps.

VF Set-up and simulation of cylinder membrane

To set up the triangular mesh of a cylinder membrane with the radius R, we first set up a circle of R on the plane z = 0 with the circle center being (0, 0, 0); next we select n vertices uniformly distributed on this circle, and thus the edge length between two nearest vertices is $l = 2R\cdot\sin(\pi/n)$; then we repeatedly move these n vertices along z axis by $\Delta z = +\sqrt{3}l/2$ and rotate along z axis by $+\pi/n$ rad. Through this process, we can get a perfect smooth triangular mesh with all the triangles being equilateral and identical in size, Fig. S12A (ESI†).

The mechanical description of the cylinder membrane is the same as the vesicle above, with the same regularization scheme

and energy minimization method, except that the volume constraint is excluded. For the mesh boundary conditions,[48] the two ends of the cylinder membrane are constrained by periodic boundary conditions (PBC), which we found provided more stable energetics even for small cylinders (R = 10 nm) at all cylinder lengths, compared with fixed boundary conditions. Periodic boundaries are also a more accurate physical representation of the experimental tether which is about 6 μm in length, because they are not pinned to a nanoscopic size (L = 55 nm). PBC is enforced by introducing ghost vertices and ghost faces, as illustrated in Fig. S12B (ESI†). The ghost vertices and ghost faces are necessary to calculate the nodal force on each of the boundary vertices. The update of the ghost vertex position relies on the boundary vertices of the cylinder. Note the integral of the membrane area and energy doesn't include the ghost faces. The protein binding on the cylinder membrane generates a local bulge (Fig. 7A), similar to the binding to vesicles (Fig. 1D), and we verified that the length of the cylinder doesn't affect the energetics of the membrane, Fig. S12C (ESI†).

VG Experimental surface densities

We estimated the surface coverage of amphipathic helices on membranes for the ALPS experiments[16] and ENTH on cylinders[17] to ensure they were below 20%, consistent with the ENTH vesicle experiments.[12] These estimates are therefore only used to confirm this threshold is not passed, as additional membrane bending mechanisms can then play a role, and they are not used for any energetic calculations. For the tether experiments, the final lipid concentration is 2.5–4 μM, of which 1% are $PI(4,5)P_2$, and the total ENTH concentration is 0.2–0.5 μM.[17] Assuming 1 : 1 binding of ENTH to $PI(4,5)P_2$ and a K_D of ∼0.5–1 μM, the fraction of bound $PI(4,5)P_2$ varies from ∼20–50%, which produces a surface density of ∼0.004–0.01 proteins per nm^2, or a maximal surface coverage of ∼12%. For the ALPS experiments, the final lipid concentration is 750 μM, and the total protein concentration is 0.75 μM.[16] With maximally 80% of proteins bound to the surface,[16] the bound protein to lipid ratio is 0.0008, and for the R = 34 nm vesicle (lipid area is ∼0.7 nm^2), the protein density on the surface is ∼0.001 proteins per nm^2. Assuming a larger footprint for ALPS, surface coverage is still <4%.

Conflicts of interest

There are no conflicts to declare.

Acknowledgements

MEJ gratefully acknowledges funding from an NIH MIRA R35GM133644, and an NSF CAREER Award 1753174. We acknowledge supercomputing resources provided by ARCH at Johns Hopkins University, and the NSF-MRI funded (Award 1920103) rockfish cluster. We thank Dr Alexander Sodt and Prof Brian Camley for helpful discussions. We also thank Prof Tobias Baumgart for kindly sharing data.

References

1 H. T. McMahon and E. Boucrot, Molecular mechanism and physiological functions of clathrin-mediated endocytosis, *Nat. Rev. Mol. Cell Biol.*, 2011, **12**(8), 517–533.
2 B. L. Woods and A. S. Gladfelter, The state of the septin cytoskeleton from assembly to function, *Curr. Opin. Cell Biol.*, 2021, **68**, 105–112.
3 A. Beber, *et al.*, Membrane reshaping by micrometric curvature sensitive septin filaments, *Nat. Commun.*, 2019, **10**(1), 420.
4 C. N. Antonescu, *et al.*, Phosphatidylinositol-(4,5)-bisphosphate regulates clathrin-coated pit initiation, stabilization, and size, *Mol. Biol. Cell*, 2011, **22**(14), 2588–2600.
5 M. Jost, *et al.*, Phosphatidylinositol-4,5-bisphosphate is required for endocytic coated vesicle formation, *Curr. Biol.*, 1998, **8**(25), 1399–1402.
6 O. Fatunmbi, *et al.*, A multiscale biophysical model for the recruitment of actin nucleating proteins at the membrane interface, *Soft Matter*, 2020, **16**(21), 4941–4954.
7 J. C. Stachowiak, *et al.*, Membrane bending by protein-protein crowding, *Nat. Cell Biol.*, 2012, **14**(9), 944–949.
8 W. F. Zeno, *et al.*, Molecular Mechanisms of Membrane Curvature Sensing by a Disordered Protein, *J. Am. Chem. Soc.*, 2019, **141**(26), 10361–10371.
9 N. S. Hatzakis, *et al.*, How curved membranes recruit amphipathic helices and protein anchoring motifs, *Nat. Chem. Biol.*, 2009, **5**(11), 835–841.
10 D. J. Busch, *et al.*, Intrinsically disordered proteins drive membrane curvature, *Nat. Commun.*, 2015, **6**, 7875.
11 B. Antonny, Mechanisms of membrane curvature sensing, *Annu. Rev. Biochem.*, 2011, **80**, 101–123.
12 W. F. Zeno, *et al.*, Synergy between intrinsically disordered domains and structured proteins amplifies membrane curvature sensing, *Nat. Commun.*, 2018, **9**(1), 4152.
13 F. Campelo and M. M. Kozlov, Sensing membrane stresses by protein insertions, *PLoS Comput. Biol.*, 2014, **10**(4), e1003556.
14 T. Itoh and P. De Camilli, BAR, F-BAR (EFC) and ENTH/ANTH domains in the regulation of membrane-cytosol interfaces and membrane curvature, *Biochim. Biophys. Acta*, 2006, **1761**(8), 897–912.
15 T. Baumgart, *et al.*, Thermodynamics and Mechanics of Membrane Curvature Generation and Sensing by Proteins and Lipids, *Annu. Rev. Phys. Chem.*, 2011, **62**(1), 483–506.
16 B. Mesmin, *et al.*, Two lipid-packing sensor motifs contribute to the sensitivity of ArfGAP1 to membrane curvature, *Biochemistry*, 2007, **46**(7), 1779–1790.
17 B. R. Capraro, *et al.*, Curvature sensing by the epsin N-terminal homology domain measured on cylindrical lipid membrane tethers, *J. Am. Chem. Soc.*, 2010, **132**(4), 1200–1201.
18 B. Nepal, J. Leveritt and T. Lazaridis, Membrane Curvature Sensing by Amphipathic Helices: Insights from Implicit Membrane Modeling, *Biophys. J.*, 2018, **114**(9), 2128–2141.
19 J. Gómez-Llobregat, F. Elías-Wolff and M. Lindén, Anisotropic Membrane Curvature Sensing by Amphipathic Peptides, *Biophys. J.*, 2016, **110**(1), 197–204.

 This journal is © The Royal Society of Chemistry 2021

20 A. J. Sodt and R. W. Pastor, Molecular modeling of lipid membrane curvature induction by a peptide: more than simply shape, *Biophys. J.*, 2014, **106**(9), 1958–1969.

21 H. Cui, E. Lyman and G. A. Voth, Mechanism of Membrane Curvature Sensing by Amphipathic Helix Containing Proteins, *Biophys. J.*, 2011, **100**(5), 1271–1279.

22 F. Campelo, H. T. McMahon and M. M. Kozlov, The hydrophobic insertion mechanism of membrane curvature generation by proteins, *Biophys. J.*, 2008, **95**(5), 2325–2339.

23 F. Feng and W. S. Klug, Finite element modeling of lipid bilayer membranes, *J. Comput. Phys.*, 2006, **220**(1), 394–408.

24 R. Lipowsky, Spontaneous tubulation of membranes and vesicles reveals membrane tension generated by spontaneous curvature, *Faraday Discuss.*, 2013, **161**, 305–331; discussion 419–59.

25 P. Rangamani, K. K. Mandadap and G. Oster, Protein-induced membrane curvature alters local membrane tension, *Biophys. J.*, 2014, **107**(3), 751–762.

26 A. Sreekumari and R. Lipowsky, Lipids with bulky head groups generate large membrane curvatures by small compositional asymmetries, *J. Chem. Phys.*, 2018, **149**(8), 084901.

27 J. Zimmerberg and M. M. Kozlov, How proteins produce cellular membrane curvature, *Nat. Rev. Mol. Cell Biol.*, 2006, **7**(1), 9–19.

28 Y. Fu, *et al.*, An implicit lipid model for efficient reaction-diffusion simulations of protein binding to surfaces of arbitrary topology, *J. Chem. Phys.*, 2019, **151**(12), 124115.

29 L. C. L. Lin, N. Gov and F. L. H. Brown, Nonequilibrium membrane fluctuations driven by active proteins, *J. Chem. Phys.*, 2006, **124**(7), 074903.

30 A. Naji, P. J. Atzberger and F. L. Brown, Hybrid elastic and discrete-particle approach to biomembrane dynamics with application to the mobility of curved integral membrane proteins, *Phys. Rev. Lett.*, 2009, **102**(13), 138102.

31 O. Kahraman, *et al.*, Bilayer-thickness-mediated interactions between integral membrane proteins, *Phys. Rev. E*, 2016, **93**, 042410.

32 C. Kotsalos, J. Latt and B. Chopard, Bridging the computational gap between mesoscopic and continuum modeling of red blood cells for fully resolved blood flow, *J. Comput. Phys.*, 2019, **398**, 108905.

33 B. Antonny, *et al.*, Activation of ADP-ribosylation factor 1 GTPase-activating protein by phosphatidylcholine-derived diacylglycerols, *J. Biol. Chem.*, 1997, **272**(49), 30848–30851.

34 W. Helfrich, Elastic Properties of Lipid Bilayers - Theory and Possible Experiments, *Z. Naturforsch., C: J. Biosci.*, 1973, **28**(11-1), 693–703.

35 M. Gleisner, *et al.*, Epsin N-terminal Homology Domain (ENTH) Activity as a Function of Membrane Tension, *J. Biol. Chem.*, 2016, **291**(38), 19953–19961.

36 W. Rawicz, *et al.*, Effect of Chain Length and Unsaturation on Elasticity of Lipid Bilayers, *Biophys. J.*, 2000, **79**(1), 328–339.

37 L. Ma and W. S. Klug, Viscous regularization and r-adaptive remeshing for finite element analysis of lipid membrane mechanics, *J. Comput. Phys.*, 2008, **227**(11), 5816–5835.

38 J. A. Szule, N. L. Fuller and R. Peter Rand, The Effects of Acyl Chain Length and Saturation of Diacylglycerols and Phosphatidylcholines on Membrane Monolayer Curvature, *Biophys. J.*, 2002, **83**(2), 977–984.

39 J. B. Larsen, *et al.*, How Membrane Geometry Regulates Protein Sorting Independently of Mean Curvature, *ACS Cent. Sci.*, 2020, **6**(7), 1159–1168.

40 R. Dimova, Recent developments in the field of bending rigidity measurements on membranes, *Adv. Colloid Interface Sci.*, 2014, **208**, 225–234.

41 R. P. Bradley and R. Radhakrishnan, Curvature-undulation coupling as a basis for curvature sensing and generation in bilayer membranes, *Proc. Natl. Acad. Sci. U. S. A.*, 2016, **113**(35), E5117–E5124.

42 A. Goychuk and E. Frey, Protein Recruitment through Indirect Mechanochemical Interactions, *Phys. Rev. Lett.*, 2019, **123**(17), 178101.

43 R. Phillips, *et al.*, Emerging roles for lipids in shaping membrane-protein function, *Nature*, 2009, **459**(7245), 379–385.

44 M. Akamatsu, *et al.*, Principles of self-organization and load adaptation by the actin cytoskeleton during clathrin-mediated endocytosis, *eLife*, 2020, **9**, e49840.

45 H. Turlier, *et al.*, Equilibrium physics breakdown reveals the active nature of red blood cell flickering, *Nat. Phys.*, 2016, **12**(5), 513–551.

46 M. Varga, *et al.*, NERDSS: a nonequilibrium simulator for multibody self-assembly at the cellular scale, *Biophys. J.*, 2020, **118**(12), P3026–P3040.

47 M. Simunovic, *et al.*, Curving Cells Inside and Out: Roles of BAR Domain Proteins in Membrane Shaping and Its Cellular Implications, *Annu. Rev. Cell Dev. Biol.*, 2019, **35**, 111–129.

48 F. Cirak, M. Ortiz and P. Schröder, Subdivision surfaces: a new paradigm for thin-shell finite-element analysis, *Int. J. Numer. Meth. Eng.*, 2000, **47**(12), 2039–2072.

49 J. Nocedal and S. J. Wright, *Numerical optimization*, New York, NY, Springer, 2006.